The Astrophysical Journal, 980:127 (19pp), 2025 February 10 https://doi.org/10.3847/1538-4357/ada60d

Spectral Variations across Latitudes on Asteroid (3200) Phaethon

M. Angrisani[1], E. Palomba[2], A. Longobardo[2], E. Rognini[3], A. Migliorini[2], E. D'Aversa[2], G. Pratesi[4], C. Gisellu[1], F. Dirri[2], L. Piazzo[5], and T. Arai[6]
[1] INAF-IAPS Rome, Italy, Via Fosso del Cavaliere, 100 Rome; Sapienza University of Rome, Italy; marianna.angrisani@inaf.it
[2] INAF-IAPS Rome, Italy, Via Fosso del Cavaliere, 100 Rome, Italy
[3] ASI Space Science Data Center (SSDC), Via del Politecnico, 00133 Rome, Italy
[4] Department of Earth Sciences, University of Firenze, Via G. La Pira 4, 50121, Florence, Italy
[5] Department of Information Engineering, Electronics and Telecommunications (DIET), "La Sapienza", University of Rome, 00184 Rome, Italy
[6] Planetary Exploration Research Center (PERC), Chiba Institute of Technology, Chiba 275-0016, Japan
Received 2024 April 22; revised 2024 December 27; accepted 2025 January 2; published 2025 February 7

Abstract

3200 Phaethon is a near-Earth asteroid known to be actively emitting dust and gas when near its perihelion, and it is the target of the Japanese DESTINY+ mission. Several visible–near-IR spectra were obtained of Phaethon during 2003–2017, which have been collected together and analyzed with respect to its shape model. Using a thermal model, we examine the diurnal temperature variations across Phaethon's surface ($\Delta T \sim 600$ K). We find different solar radiation heating between the north and south regions, with very high surface temperatures in the south region (max peak ~ 1050 K), while a lower temperature is found in the north region (a mean value of 760 K). Our analysis of the photometrically corrected slope suggests a latitudinal trend in surface composition. We propose that the northern region of Phaethon may be linked to unusual chondrites and naturally heated Y-82162 samples (63–125 μm and/or chips), while the southern region shows similarities to Ivuna CI chondrites heated to 700°C (0–125 μm). The equatorial region appears to include a mixture of materials from both hemispheres.

Unified Astronomy Thesaurus concepts: Asteroids (72); Small Solar System bodies (1469); Spectroscopy (1558); Meteorites (1038)

1. Introduction

The active asteroid (3200) Phaethon is the target of the upcoming Demonstration and Experiment of Space Technology for Interplanetary Voyage with Phaethon Flyby and Dust Science (DESTINY+) mission, scheduled for launch in 2025, with a planned flyby of Phaethon in 2028 January (T. Arai et al. 2023). A comprehensive understanding of this asteroid prior to the mission is essential for effective planning and execution.

From 2003 to 2017, several observation campaigns were conducted to study Phaethon at various times and using different telescopes in the visible (VIS)–near-IR (NIR) range (Licandro et al. 2007; Kareta et al. 2018; E. Palomba et al. 2018; M. Lazzarin et al. 2019; Lee et al. 2019). These campaigns observed Phaethon under varying phase angles, but no significant spectral features were detected, with the exception of a "weak" absorption band around 0.43 μm reported by M. Lazzarin et al. (2019). All spectra exhibit a negative slope, with some showing a steeper gradient, which might indicate variations in the degree of depletion or transformation of near-surface material due to the extreme temperatures Phaethon experiences during perihelion (0.14 au; K. Ohtsuka et al. 2009) or other surface heterogeneities.

Phaethon is classified as a B-type asteroid (F. De Meo et al. 2009), typically linked to dehydrated CI/CM chondrites. The spectral features of CI/CM chondrites are altered from hydrated C type to B type by thermal metamorphism (Hiroi et al. 1996). C-type asteroids, which can include a significant proportion of volatile-rich materials such as phyllosilicates (clays) or other hydrated minerals, have been suggested as components of Phaethon (Licandro et al. 2007; K. Ohtsuka et al. 2009; M. Lazzarin et al. 2019). However, the absence of a 3 μm hydration feature (Takir et al. 2020) indicates that Phaethon does not have hydrated minerals on its surface.

Phaethon has a distinctive top-shaped structure with an estimated effective diameter of 5.1 ± 0.2 km and a rotation period of approximately 3.6 hr (J. Hanuš et al. 2018). Radar images suggest that Phaethon's shape includes an equatorial ridge, similar to other observed near-Earth asteroids, with several surface features hundreds of meters in extent. Notable features include a possible crater over 1 km across and a roughly 600 m radar-dark region near one of the poles (Taylor et al. 2019). Its geometric albedo, derived from thermophysical modeling (TPM), is approximately $pV \approx 0.13$ (J. Hanuš et al. 2016; Masiero et al. 2019). Thermal inertia modeling (600 ± 200 J m^{-2} K^{-1} s$^{-1/2}$) suggests a surface particle size of 1–2 cm (J. Hanuš et al. 2016, 2018).

To support the mission preparation and assess whether the spectral variability observed in ground-based studies corresponds to actual surface heterogeneities on Phaethon, we have compiled and analyzed existing VIS–NIR spectral data collected over the past 20 yr (Section 2). To determine if this variability is driven by thermal processes, we employ a specific thermal model based on the shape model by J. Hanuš et al. (2018; Section 3) to estimate Phaethon's surface temperature distribution (Section 4).

By retrieving the footprints of the ground-based spectra (Section 5) in relation to the current Phaethon shape model, we are able to apply photometric corrections, facilitating a more accurate comparison of the measurements. This approach aims to verify potential latitudinal variations (Section 6). The results of this analysis are discussed in Section 7, followed by our conclusions in Section 8.

Table 1
Observations from 2003 to 2017 of (3200) Phaethon

Date of Observation	Telescope	Phaethon Distance from the Sun	Airmass Range	Authors
2003 Nov 14	WHT	∼1.16 au	1.20	J. Licandro et al. (2007)
2007 Nov 5	Tillinghast	∼1.43 au	1.22–1.0	T. Kareta et al. (2018)
2017 Dec 7	BOAO	∼1.16 au	…	H. J. Lee et al. (2019)
2017 Dec 16–17	TNG	∼1.02–1.01 au	1.07–1.12	M. Lazzarin et al. (2019)
2017 Dec 19	TNG	∼1.02 au	1.18–1.20	E. Palomba et al. (2018)

2. Data

The set of VIS–NIR Phaethon observations from ground-based telescopes gathered for the present work is listed in Table 1 (Licandro et al. 2007; Kareta et al. 2018; E. Palomba et al. 2018; M. Lazzarin et al. 2019; Lee et al. 2019). All normalized spectra are shown in Figures 1–3.

Licandro et al. (2007) observed Phaethon with the William Herschel Telescope (WHT) on 2003 November 14, using the ISIS spectrograph. They found a spectral variability suggesting an inhomogeneous composition and/or a variegation in the physical properties (particle size, etc) of the surface. They also indicated a link to carbonaceous chondrite meteorites.

Kareta et al. (2018) conducted optical observations from 0.4 to 0.74 μm on 2007 November 5 (UTC) from the Tillinghast 1.5 m telescope on Mount Hopkins, Arizona, using the high-throughput FAST spectrograph. The spectra spanned nearly a full rotation and they are blue-sloped throughout the visible wavelengths, with subtle slope variations.

The 2017 December Phaethon Earth approach was a very important event, since the asteroid was about 10 times closer with respect to previous apparitions. Observations from Lee et al. (2019) were performed at Mt. Bohyunsan Optical Astronomy Observatory (BOAO) in South Korea using the 1.8 m telescope on 2017 December 7. Their results were consistent with previous studies that found Phaethon to be a B-type asteroid (Binzel et al. 2001; F. De Meo et al. 2009). Lee et al. (2019) found that Phaethon's southern hemisphere has a homogeneous surface. However, they used the pole solution and shape model from Kim et al. (2018) and assumed that the spectral slope was independent of the phase angle. This assumption is not accurate, as demonstrated by Fornasier et al. (2020). E. Palomba et al. (2018) observed the asteroid, on the night of December 19, at the 3.5 m Telescopio Nazionale Galileo (TNG) in the VIS–NIR spectral interval (0.4–2.5 μm), obtaining three spectra in the visible from 0.4 to 0.8 μm, with a strong fringing longward of 0.8 μm, which does not allow the use of the data between 0.8 and 1 μm. M. Lazzarin et al. (2019) also observed Phaethon during the nights of 2017 December 16 and 17 using the 1.22 m Galileo Telescope of the Department of Physics and Astronomy of the University of Padova in Asiago, Italy. They observed a weak absorption band around 0.43 μm and a significant variation in the UV spectral slope.

3. Shape Model Properties

The shape model used in this study is based on the work of J. Hanuš et al. (2018). This model was derived using an optical data set consisting of 55 light curves from the DAMIT database (Ďurech et al. 2010), which had already been utilized for shape model determination in J. Hanuš et al. (2016). Additionally, four light curves obtained in 2016 by B. D. Warner (2017), four light curves by David Polishook (from apparitions in 2005, 2007, and 2017), and four more light curves from the apparition in 2017 December were also included (J. Hanuš et al. 2018). Notably, our VIS–NIR spectral data fall within the coverage of these light curves, allowing us to establish an uncertainty of 10° in the sub-Earth/solar position derived from the model (Ďurech et al. 2010; J. Hanuš et al. 2011).

Meanwhile, a preliminary shape model (S. E. Marshall et al. 2021) has been developed using a combination of light-curve observations from 16 apparitions (1989–2019) and radar data from both the Arecibo Observatory (collected in 2007 and 2017) and the Goldstone Deep Space Communications Complex (from 2017). A publication detailing this final shape model is currently in preparation.

The updated shape model has a modeled rotation period ($P_{\rm rot} = 3.603955$ hr) and a spin-axis orientation (ecliptic longitude $\lambda = 316°$ and latitude $\beta = -48.^{\circ}7$) that are consistent with the convex model proposed by J. Hanuš et al. (2018). This model, constrained by radar observations, suggests a mean (volume-equivalent) diameter of approximately 5.38 km, slightly larger than the estimate provided by J. Hanuš et al. (2018; 5.1 km).

For the purposes of this paper, a highly accurate shape model is not essential, as ground-based telescope observations capture the entire asteroid disk, often with varying percentages of illumination, resulting in the loss of small-scale surface details.

4. Phaethon Thermal Model

A near-Earth asteroid thermal model (NEATM) has been developed by A. W. Harris (1998) and has proven to be suitable for estimating the asteroid's diurnal temperatures. However, NEATM assumes that there is no nightside emission ($T_{\rm night} = 0$ K), very low thermal inertia, $\Gamma = 0$ (implying a smooth surface), and/or a nonrotating body ($\omega = 0$). Therefore, in order to determine the surface temperature during the day–night cycle, we employ a more complete TPM, aimed at solving the heat conduction equation and providing theoretical surface temperatures as a function of conductivity, albedo, emissivity, density, and specific heat. We applied such a one-dimensional model to the detailed shape model of Phaethon (J. Hanuš et al. 2018) in order to take into account the instantaneous illumination. The shape is associated with pole ecliptic coordinates (λ, β) = (318°, −47°), with an error of ±5°.

The surface temperature is given by the following equation:

$$\frac{S_0(1 - A)\cos(\theta)}{\mathrm{r}^2} - \epsilon\sigma T^4 = -k\frac{\partial T}{\partial x}, \quad (1)$$

where A is the bolometric Bond albedo; $S_\circ$ is the solar constant, the solar flux at 1 au, ∼1366 Wm^{-2}; θ is the solar incidence angle; r is the heliocentric distance in astronomical units; ϵ is the infrared emissivity; σ is the Stefan–Boltzmann constant,

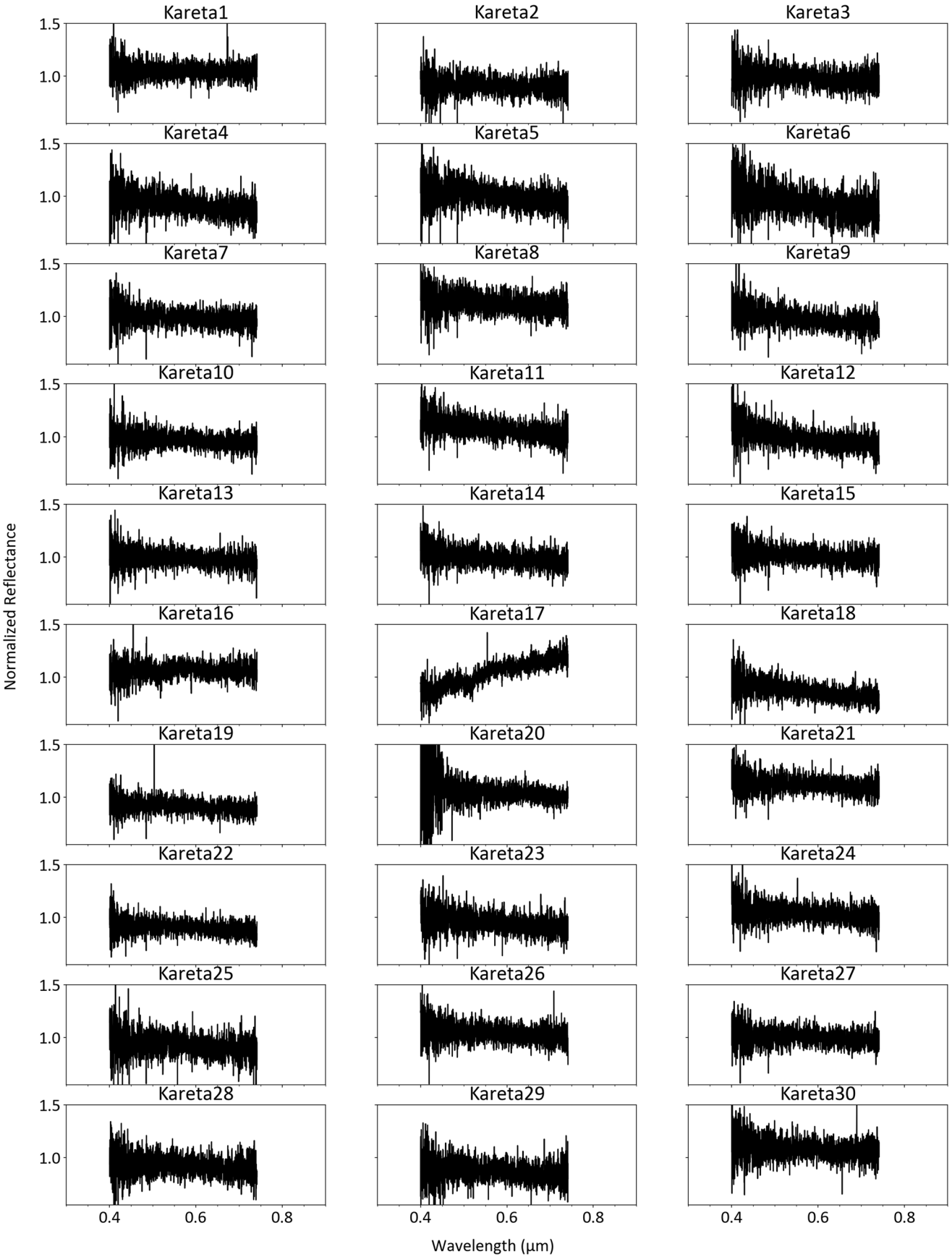

Figure 1. Normalized spectra shared by Kareta et al. (2018). The number of spectra presented here is greater than in the original publication, where they were averaged over every three spectra. We have excluded Spectrum 17 from our analysis, due to its anomalous nature compared to the other data points.

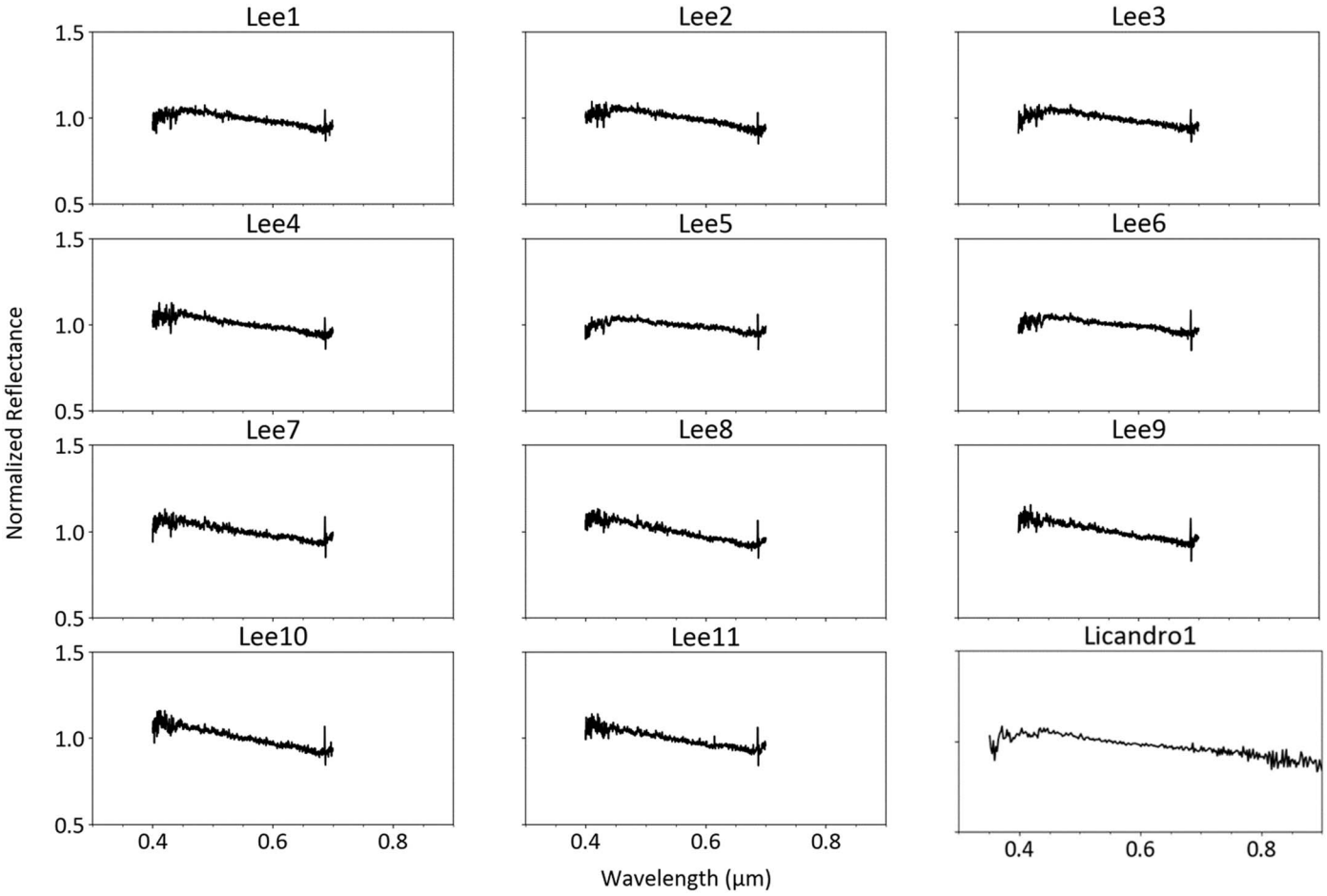

Figure 2. Normalized spectra shared by Lee et al. (2019) and spectrum shared by Licandro et al. (2007; last plot).

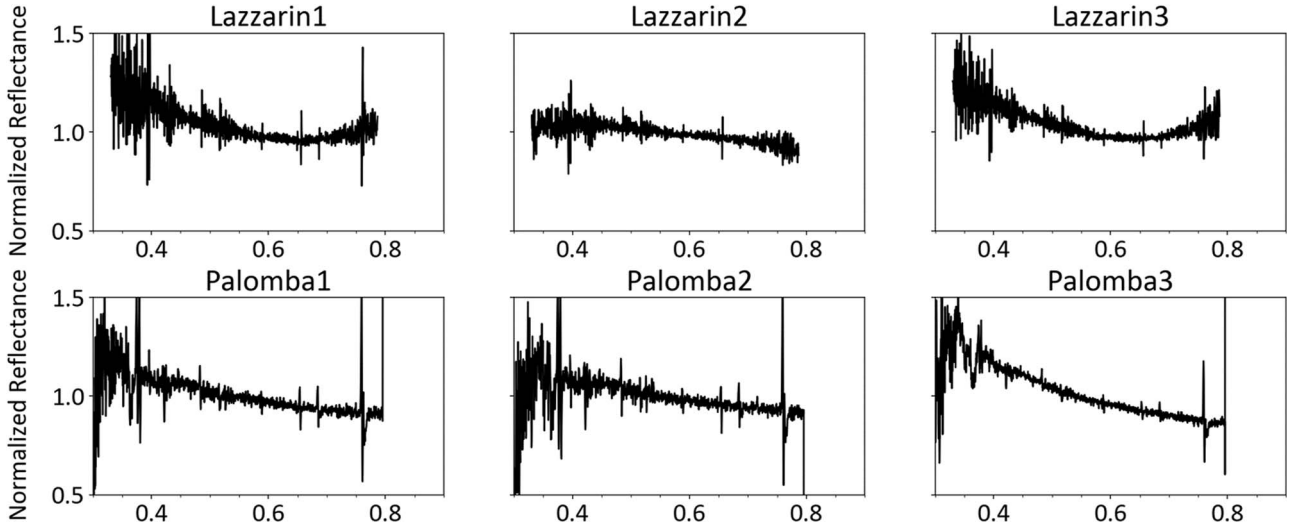

Figure 3. Spectra shared by M. Lazzarin et al. (2019; top) and E. Palomba et al. (2018; bottom).

$5.671 \times 10^{-8}\,\mathrm{Wm^{-2}\,K^{-4}}$; k is the thermal conductivity; and $\frac{\partial T}{\partial x}$ is the vertical gradient of the temperature at the surface. The presence of this last term requires the solution of the one-dimensional heat equation, as follows:

$$\rho c \frac{\partial T}{\partial t} = \frac{\partial}{\partial x}\left(k \frac{\partial T}{\partial x}\right), \tag{2}$$

where ρ is the density, c is the specific heat, t is the time, and x is the depth. In this work, the density, the specific heat, and the thermal conductivity are assumed to be constant.

The distance (r) from the Sun was taken from the JPL Small-body Database.[7] The infrared emissivity was assumed to be 0.9,

[7] https://ssd.jpl.nasa.gov/horizons/app.html#/

while the geometric albedo (pv) is related to the effective Bond albedo (A) of the asteroid surface, by $A = (0.290 + 0.684\,G)\,pv$, where G is the asteroid phase parameter (E. Bowell 1989, B. Rozitis et al. 2013; Lee et al. 2019). We use $G = 0.15 \pm 0.03$ and $p_v = 0.12 \pm 0.01$ (J. Hanuš et al. 2016; Lee et al. 2019). The thermal inertia assumed in this work is $600 \pm 200\,\mathrm{J\,m^{-2}\,s^{-0.5}\,K^{-1}}$ (J. Hanuš et al. 2018).

The angle of solar incidence $\boldsymbol{\theta}$ on a facet is derived from the scalar product:

$$\cos(\theta) = \boldsymbol{n}\cdot\boldsymbol{n}, \tag{3}$$

where $\boldsymbol{n}$ and $\boldsymbol{n}_{\mathbf{Sun}}$ are, respectively, the direction of the facet surface vector (obtained from the shape model) and the direction of the Sun in the shape model reference (derived using the subsolar point).

The TPM output is presented in Figure 4, which shows the calculated Phaethon surface temperature approximal at its perihelion. The maximum model temperature uncertainty is ±35 K. It is calculated as half of the absolute value of the discrepancy between the temperature estimated with thermal inertia of 600 and $400\,\mathrm{J\,m^{-2}\,s^{-0.5}\,K^{-1}}$.

Taylor et al. (2019) have suggested that Phaethon's albedo could be 0.105 or lower, based on radar observations, compared to the value reported by J. Hanuš et al. (2016). However, the temperature differences modeled using this albedo value and ours are smaller than the model's estimated error, making this variation negligible.

From Figure 2, Phaethon can reach a sufficiently high temperature for surface dehydration and decomposition of minerals due to solar radiation, with the maximum global temperatures at the dayside (≈1050 K) found at ∼0°–30° latitudes and decreasing toward the poles, while the minimum peak of the temperature on the nightside is found to be ≈300 K. Because of this temperature, it is also improbable that water ice is preserved on Phaethon's surface. Using the thermal metamorphism condition of CI/CM chondrites proposed by T. Nakamura (2005), we can distinguish different regions on Phaethon's surface at the dayside during the perihelion: the ∼0°–30° latitude region is at Stage IV (approximately 1023–1273 K), where T. Nakamura (2005) found that crystalline secondary olivine and troilite occur in CI/CM chondrites. Moving toward the south pole, the south region is at Stage III (approximately 773–1023 K), where low-crystalline secondary olivine and troilite exist in a matrix characterized by amorphous silicates and relicts of poorly crystalline phyllosilicates. The nonilluminated sides (or night-sides) are roughly at Stage II (523–773 K) and Stage I (<573 K), where the serpentine becomes amorphous, but the matrix shows the occurrence of primary olivine. No tochilinite exists, but newly created troilite with low crystallinity exists (T. Nakamura 2005).

5. Retrieval of the Observation Geometry

In order to understand if the observed spectral variability can be associated with real Phaethon surface heterogeneities, we investigated the surface portion effectively probed by each observation using the shape model by J. Hanuš et al. (2018). We computed the geometry of the observation based on the pole solution of J. Hanuš et al. (2016, 2018) that corresponds to the pole ecliptic coordinates $(\lambda, \beta) = (318, -47)$. Using the sky projection of the Astronomical Institute of Charles University[8] (Ďurech et al. 2010), we computed the sub-Earth and subsolar coordinates and the solar phase angle on the asteroid surface for each epoch.

In addition, we estimated the illuminated and visible portions of the asteroid. Here, the illuminated fraction, k, is the ratio of the luminous area to the total area of the disk, as seen from the Earth, given by

$$k = 0.5 \quad (1 + \cos g), \tag{4}$$

where g is the solar phase angle. The geometric parameters are summarized in Table 2.

Radar images have revealed surface features on Phaethon that span hundreds of meters (Taylor et al. 2019). Taylor et al. (2019) identified two major radar features: a topographically low area—possibly a concavity or crater, located below 30° latitude—and a dark spot at the north pole, likely representing a flatter region compared to its surroundings. Additionally, a brighter region, which may indicate a boulder or raised topography larger than approximately 300 m, was also observed. Other less distinct features include a candidate concavity near the equator and ridge lines below about 10° latitude that contribute to the dark–bright variations seen in the radar images, as well as a linear facet along the equator that appears slightly elevated above its surroundings. However, our analysis suggests that it is challenging to conclusively attribute the observed heterogeneity to these morphological features. It is important to note that Earth-based observations cover only a portion of the surface, with the percentage of illumination varying according to the phase angle between the Sun and the observer. Consequently, detecting features that span only a few kilometers on the surface can be difficult.

For these reasons, and in accordance with the findings of E. MacLennan et al. (2022), who identified a potential hemispherical heterogeneity, we divided Phaethon into three regions (Figure 5): the northern latitudes (greater than +10°), the equatorial region (approximately −30° to +10°), and the southern latitudes (less than −30°). Then, using the sub-Earth coordinates, we attempted to correlate these regions with the possible observer (Table 2). The specific coordinates for each spectrum are provided in the Appendix (Table A1).

6. Spectral Analysis and Results

It is worth noting that besides the different geometric conditions detailed above, all spectra were obtained at different perihelion passages and at different observing conditions and calibrations (e.g., instrumentation and solar analog stars, etc). In order to better compare the observed spectral shapes, we low-pass-filtered all spectra with a boxcar average function with a width of 20 nm, then we normalized them to 0.55 if they had not already been standardized to this value. In the absence of particular absorption features in the reflectance spectrum, the spectral slopes between 0.55–0.7 μm and 0.4–0.55 μm are used as parameters to search for relevant variations of the regolith across the asteroid's surface. The slopes were fitted with a linear model between two fixed-wavelength boundaries (taking advantage of the SciPy "curve_fit" routine; P. Virtanen et al. 2020). The normalization process and the application of spectral slope retrieval effectively minimized the influence of several parameters. Specifically, incidence and emission angles, which typically act as wavelength-independent multiplicative factors for dark bodies (e.g., A. Longobardo et al. 2019, 2022), are mitigated. Similarly, variations in coverage, also a multiplicative factor, are accounted for (e.g., Longobardo et al. 2016).

[8] https://astro.troja.mff.cuni.cz/projects/damit/

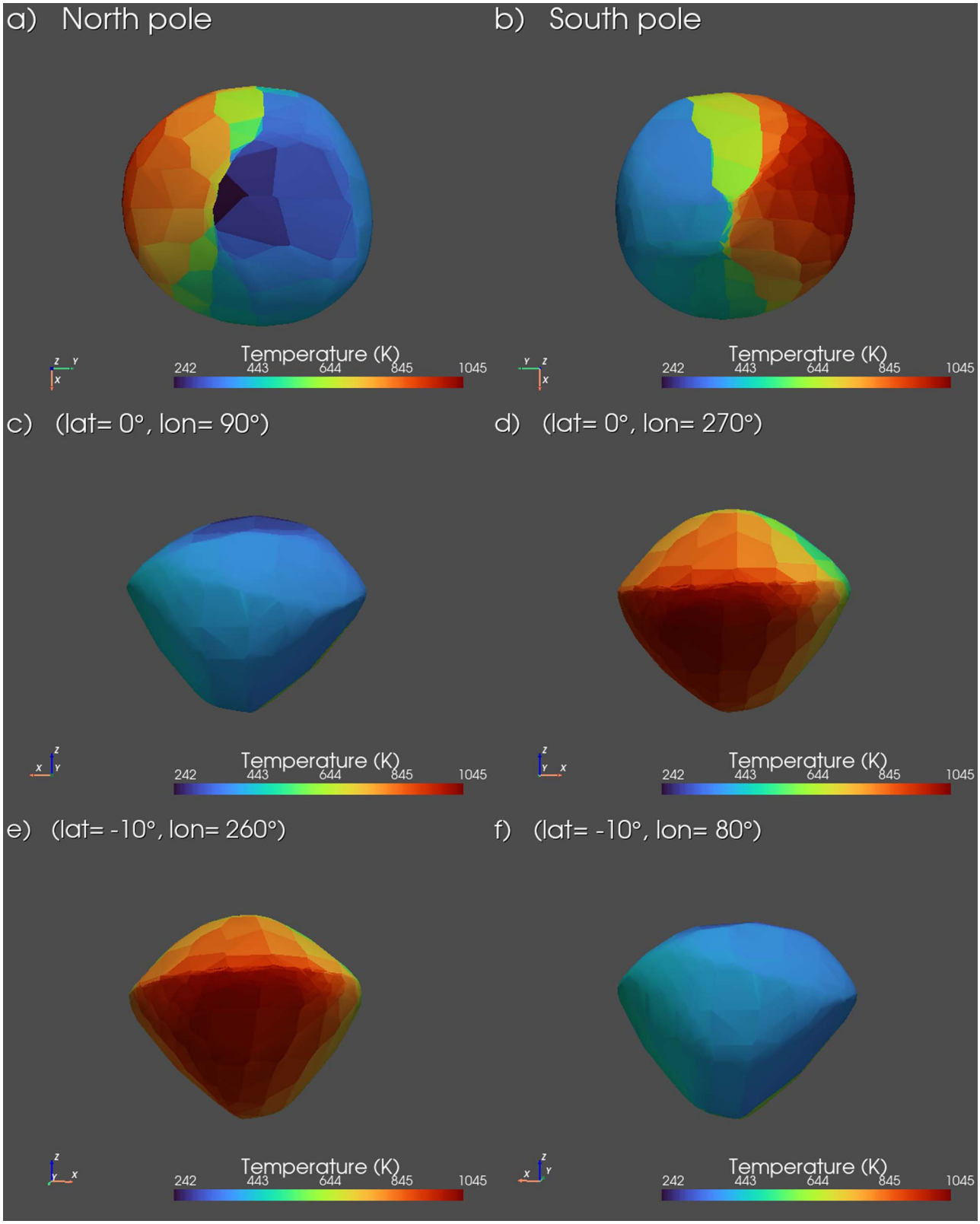

Figure 4. Phaethon surface temperature at the perihelion, considering the surface thermal inertia, $\Gamma = 600$ Jm^{-2} s$^{-0.5}$ K^{-1}, and a rotation period, P = 3.6 hr. Thus, the color bar shows the temperature. (a) and (b) The nadirs from the north and south poles. (c) and (d) The views from (LAT, LON) = (0°, 90°) and (0°, 270°), respectively. (e) and (f) The views from (−10°, 260°) and (−10°, 80°) to show the subsolar point at the perihelion.

Additionally, this work models the dependence on phase angle, further reducing its impact.

Due to the uncertainty in the sub-Earth coordinates, we decided to average the spectral slope within every 30° longitude bin for each observer while keeping the latitude fixed. This approach was chosen because observers such as Kareta et al. (2018) and Lee et al. (2019) were able to observe Phaethon throughout its entire rotation while maintaining a

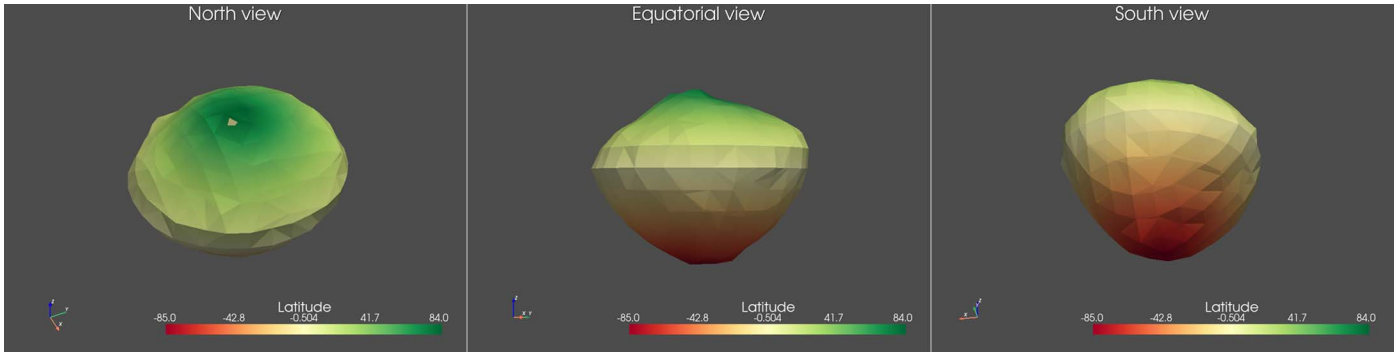

Figure 5. Visualization of the shape model of Phaethon from the north, equatorial, and south viewpoints.

Table 2
Subdivision of Phaethon's Regions Along with Corresponding Observations

	Observer	Phase Angle (deg)	Illumination Fraction (%)	Possible Radar Features
North	Kareta et al. (2018)	41°	88%	Polar dark spot (e)
(+10°N < x < +90)	Lee et al. (2019)	21°	97%	Linear facet (d)
Equatorial	Licandro et al. (2007)	57°	77%	Candidate boulder (a), candidate concavity (c)
(−30°N < x < 10°N)	M. Lazzarin et al. (2019)	63°–77°	73%–62%	
South	E. Palomba et al. (2018)	101°	40%	Candidate concavity (b)
(−90° < x < −30°N)				

Note. Each region is associated with the observer(s) who probably observed it, the phase angle, the fraction of the illuminated region, and possible morphological features based on Taylor et al. (2019).

constant latitude, unlike other observers, who focused on specific portions of Phaethon. The error is calculated as the standard deviation of the data within the bin for samples with multiple data points. If there is only a single data point in the bin, the error is approximated as three times the uncertainty derived from the smoothing and slope calculations.

We then performed a photometric correction, i.e., the removal of the influence of viewing angles, avoiding misinterpretation of the surface due to photometric effects. We applied the empirical procedure adopted by A. Longobardo et al. (2019; 2022), consisting of retrieving the slope S at different phase angles, obtaining the phase-reddening coefficient γ (i.e., the angular coefficient of the linear fit between the spectral slope and phase angle), and retrieving the photometrically corrected slope S' (calculated at a phase angle of 30°) by applying the relation

$$S' = S - (\gamma \times (g - 30°)), \quad (5)$$

where S is the measured slope and g is the phase angle of the observation.

Accordingly, the spectral phase reddening in the ∼0.55–0.7 μm range was computed. As shown in Figure 6 (right), the slope shows a positive linear correlation with phase angle up to about 77°, while at higher phase angles the slope decreases to the same values measured at 20°. Since it is quite common for spectral slopes measured at phase angles larger than 80°–90° to not follow the same linear behavior observed at lower phase angles (e.g., A. Longobardo et al. 2017; Fornasier et al. 2020), the observations at 101° have been excluded from the linear fit used to retrieve the phase-reddening coefficient. The spectral slope, from phase angles of 21° to 77°, increases with a 0.55–0.7 μm phase-reddening coefficient of $\gamma = (5.0 \pm 1.7) \times 10^{-3}\ \mu\mathrm{m}^{-1}\ \mathrm{deg}^{-1}$ while the phase reddening evaluated in the 0.40–0.55 μm range decreases with a reddening coefficient of $\gamma_2 = (-8.2 \pm 1.3) \times 10^{-3}\ \mu\mathrm{m}^{-1}\ \mathrm{deg}^{-1}$ (Figure 6).

To validate the spectral slope behavior, we compared our result with other small bodies. While several physical and optical parameters can, in principle, influence this behavior, albedo is generally the primary driver of photometric properties (Longobardo et al. 2016), particularly phase reddening (A. Longobardo et al. 2022). To assess the results, we compared them to those for Ceres, which has an albedo of 0.090 ± 0.003 (J.-Y. Li et al. 2006), similar to that of Phaethon (0.122 ± 0.008, as reported by J. Hanuš et al. 2016, 2018; or 0.105, according to Taylor et al. 2019). M. Ciarniello et al. (2017) calculated Ceres's spectral slope between 0.55 and 0.8 μm, finding a value of $4.6 \times 10^{-3}\ \mu\mathrm{m}^{-1}\ \mathrm{deg}^{-1}$, which is comparable to the phase reddening (0.55–0.7 μm) obtained for Phaethon at phase angles lower than 80°. Therefore, it is reasonable to apply our result for the photometric correction.

The observation at 101° is included in the scatter plot of slope versus sub-Earth coordinates (Figure 7) because, typically, the slope increases at higher phases due to photometric effects like phase reddening. However, the detection of a bluer spectrum at higher phases indicates a genuine change in the slope, rather than an artifact caused by phase reddening (M. Ciarniello et al. 2017). In the wavelength range of approximately 0.55–0.7 μm, the photometrically corrected slope shows no significant variation with sub-Earth coordinates (bottom panels of Figure 7). In contrast, in the 0.4–0.55 μm range, the photometrically corrected slope appears to become redder with increasing latitude (top left panel of Figure 7).

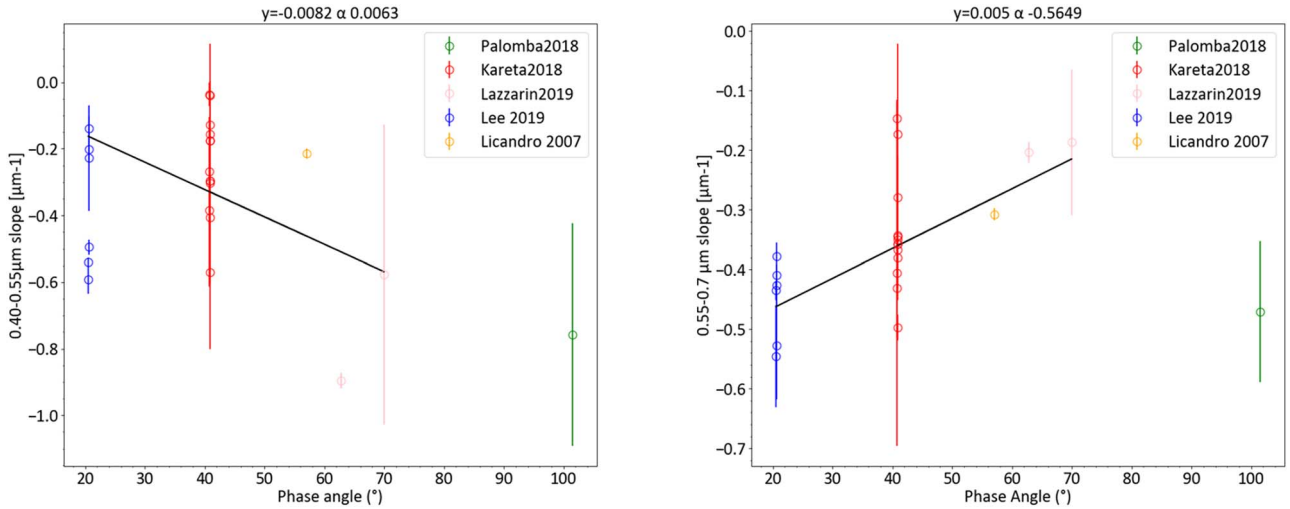

Figure 6. Phase reddening in spectral slopes evaluated in the 0.40–0.55 μm range (left) and the 0.55–0.7 μm range (right) from 20.°6 to 76.°6. The black line is the linear fit for a phase angle lower than 100°.

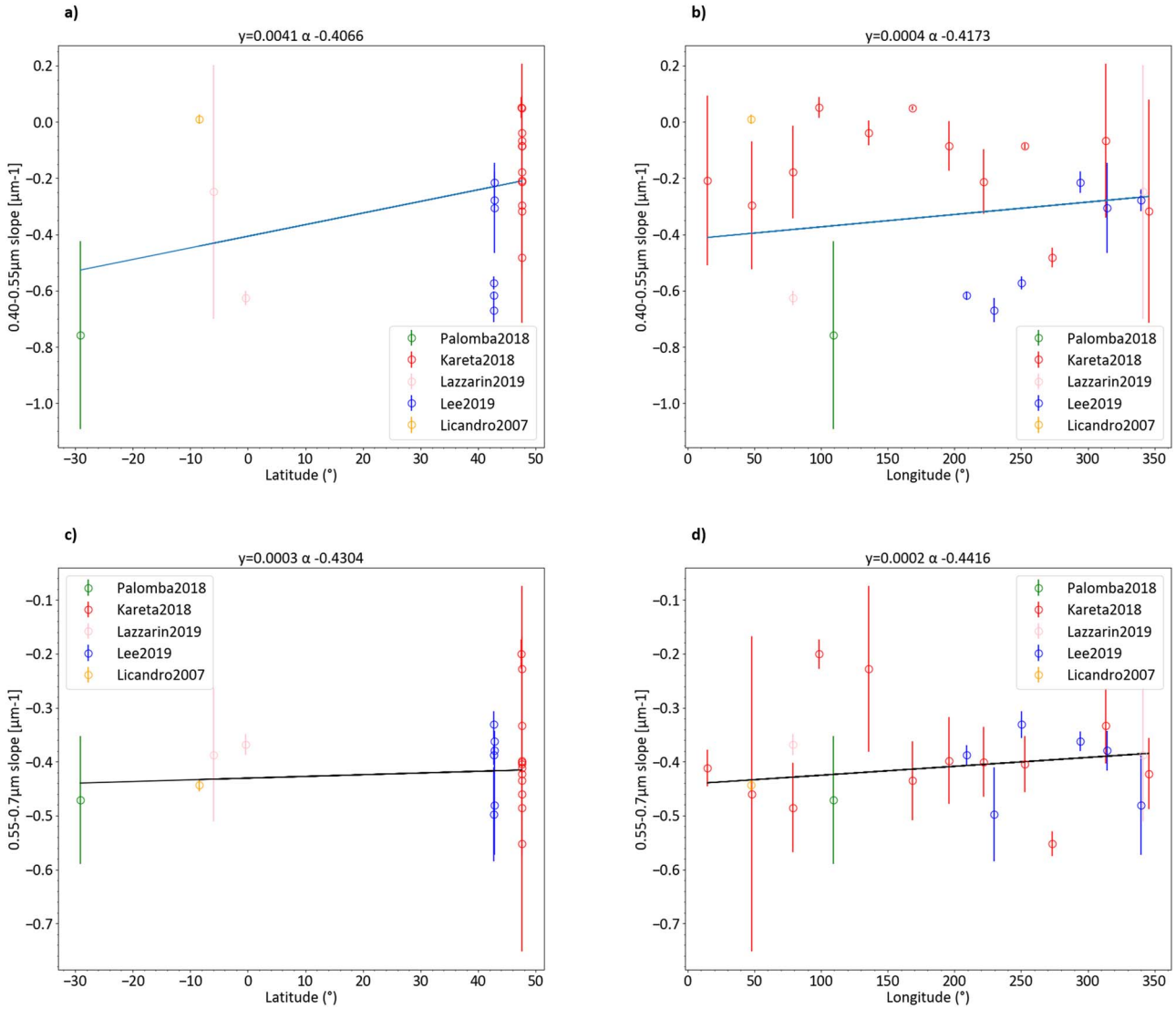

Figure 7. Spectral slope variation across latitude and longitude. Top: spectral slope in the 0.4–0.55 μm range as a function of latitude (left) and longitude (right). Bottom: spectral slope in the 0.55–0.7 μm range as a function of latitude (left) and longitude (right).

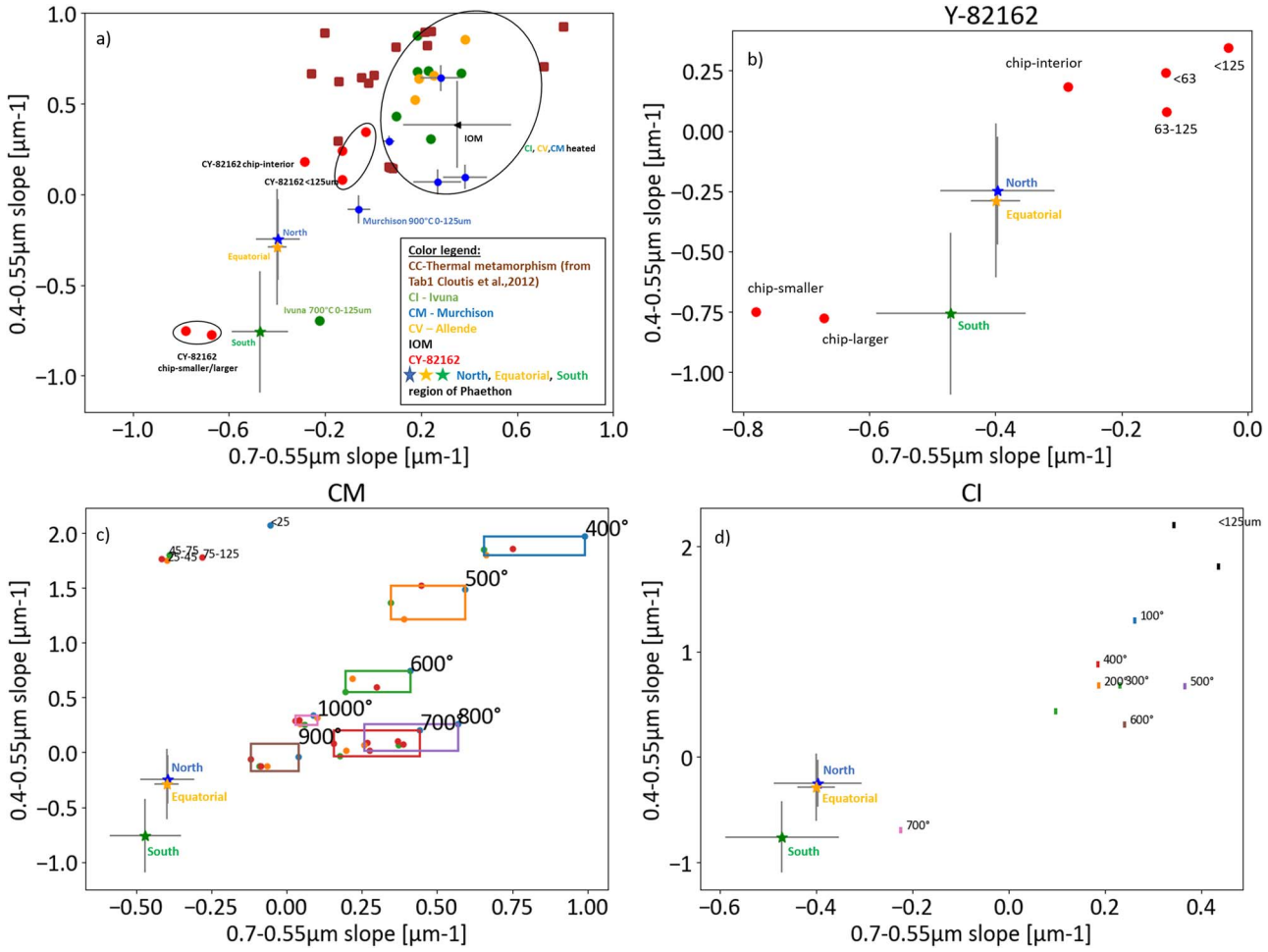

Figure 8. Comparison of Phaethon median slope regions (north, equator, and south) with meteorites from RELAB. The error bars for Phaethon represent the standard deviation of the slope within the specified regions. The meteorite error bars reflect the slope variation within the indicated cluster. (a) Comparison of the average slope of Phaethon (north, equator, and south) with the entire data set less than 1 μm^{-1}. (b) Comparison of the average slope of Phaethon (north, equator, and south) with meteorite Y-82162. (c) Comparison of the mean slope of Phaethon (north, equator, and south) with Murchison meteorite particles of varying sizes: <25 μm (blue); 25–45 μm (orange); 45–75 μm (green); and 75–125 μm (red), both fresh and heated at 400°C to 1000°C. (d) Comparison of the average slope of Phaethon (north, equator, and south) with Ivuna meteorite particles <125 μm, under different heating conditions: fresh (black); 100°C (blue); 200°C (orange); 300°C (green); 400°C (red); 500°C (purple); 600°C (brown); and 700°C (pink).

7. Discussion

The analysis of all Phaethon spectra described above shows a slight difference of the spectral slope with latitude, still present after photometrical correction. This may reflect the true spatial heterogeneity of its regolith.

To understand this, we searched for some Phaethon spectral analog. We calculated the mean values of the photometrically spectral slopes (avoiding geometry effects) associated with Phaethon's latitudinal regions (north, equatorial, and south), and we searched for and selected a set of spectral samples of carbonaceous chondrite meteorites (UV–VIS–NIR spectra taken with a phase angle of 30° from the NASA Reflectance Experiment LABoratory or RELAB). This spectra database includes CI (Ivuna fresh and heated), CM (Murchison fresh and heated), CV (Allende fresh and heated), CK (meteorites from Table 3 of E.A. Cloutis et al. 2012a), IOM, and some carbonaceous chondrites showing evidence of aqueous alteration and subsequent thermal metamorphism (from Table 1 of E.A. Cloutis et al. 2012b). A total of about 230 spectra are analyzed and spectral slopes are evaluated through the same method used for Phaethon observations. A downselection has been made, accounting for all spectra having a slope lower than 1.0 μm^{-1}. The results are shown in the scatter plot of Figure 8, together with the Phaethon mean values (Table 3).

To identify the best spectral analogs in the scatter plot (Figure 8), we calculated the Euclidean distance between the points representing Phaethon's north, equatorial, and south regions and those representing all the meteorites in our data set. This was done using Python's *math.dist()* method, where the *x*-coordinate corresponds to the slope between 0.55 and 0.7 μm, and the *y*-coordinate corresponds to the slope between 0.4 and 0.55 μm. Tables 4–6 list the top 10 closest analogs for each region.

Relying solely on slope analysis to identify an analog meteorite can be challenging, as other factors may also contribute to slope variations that are difficult to disentangle (Cloutis et al. 2011). Therefore, our conclusions are supported by integrating our VIS–NIRS slope results with findings from IR spectral analysis and thermal inertia measurements, as reported by E. MacLennan et al. (2022) and E. MacLennan & M. Granvik (2024).

Table 3
Average Spectral Slopes of Phaethon (0.4–0.55 μm and 0.55–0.7 μm) across the North, Equatorial, and South Regions

	North	Equatorial	South
0.55–0.7 μm^{-1} deg^{-1}	-0.397 ± 0.091	-0.400 ± 0.039	-0.471 ± 0.118
0.40–0.55 μm^{-1} deg^{-1}	-0.248 ± 0.223	-0.289 ± 0.320	-0.758 ± 0.334

7.1. VIS–NIRS Spectra Analysis (This Work)

Our analysis suggests that the northern and equatorial regions of Phaethon most closely resemble the Murchison meteorite, heated for one week at 900°C in a 10^{-5} atm H_2 atmosphere (top panel of Figure 9), with a particle size of 45–75 μm (or 75–125 μm if we consider the second close selection). The southern region, however, shows the closest match with Y-82162 (larger chip; bottom panel of Figure 9). Y-82162 is supposed to have been subject to 600°C–700°C for long-duration heating or 800°C for short-duration heating (Akai 1990, 1992, 1994). Caution is warranted in interpreting the Y-82162 (larger chip) match. Notably, the two Y-82162 chip points (larger and smaller chips) in the bottom left of the scatter plot are distinctly separated from Y-82162 (the chip interior), despite having compatible particle sizes, suggesting that the difference in position is likely due to compositional changes. This may be reasonably attributed to terrestrial weathering, which could have introduced new mineral phases, slightly altering the composition from its original state. Indeed, Y. Ikeda and K. Makoto et al. (1992) reported that most of the Y-82162 fusion crust was lost and some parts of the surface were coated with thin and powdery efflorescence-like material, while Hiroi et al. (2021) reported that chips of the dehydrated CI chondrite Yamato (Y)-82162 exhibited different spectral characteristics depending on the area analyzed. The spectra from the darker areas (Spot A) and those from a whitish coating (Spot B), which can easily be shaved off and is likely a result of terrestrial weathering, displayed high negative UV–VIS–NIR slopes and a complex 3 μm absorption band with three distinct peaks, differing from a sharp structural OH band at 2.71 μm. Due to these inconsistencies, both Spot A and Spot B spectra were excluded from their study. Given these considerations, we exclude from our study the Y-82162 small and large chips (cbmb19 and camb19), and we propose that the southern region of Phaethon may better match the "second-best analog"—Ivuna heated to 700°C with a particle size of <125 μm (middle panel of Figure 9). An association with heated CI meteorites is also suggested for asteroid 101955 Bennu—see Clark et al. (2011).

The two matches—Murchison heated to 900°C and Ivuna to 700°C—would suggest that the region to the north is more warmed than to the south, but it should be pointed out that the thermal model applied in this work is valid for the Phaethon configuration during the last 20 yr of observations. Indeed, J. Hanuš et al. (2016) report that when the perihelion was the lowest, about 2 kyr ago, the northern hemisphere of Phaethon (the preferred pole solution) was harshly irradiated by sunlight at perihelion (0.126 au). Furthermore, considering the possibility of material being ejected during activity, along with thermal fractures (as suggested by M. Delbo et al. 2014) and the effects of the solar wind, it is plausible that the region to the south—where the subsolar point is currently located at perihelion—remains a relatively "new" region that has not yet reached the maximum temperature of 900°C.

Indeed, the Phaethon temperature variation due to the illumination cycle can induce thermal fatigue of the surface material, resulting in mechanical stresses that affect regolith production. The efficiency of this thermal fragmentation is dominated by the amplitude of the temperature cycles and by the temperature change rate (K. Hall and M.-F. André 2001), which in turn depend on the heliocentric distance, rotation period, and surface thermal inertia.

On Phaethon, strong temperature variations (even $\delta T\max \sim 600$ K, if we consider the diurnal excursion shown in Figure 2) are now expected in association with the ~3.6 hr rotation period. Following the argument of D. Jewitt and J. Li (2010), the stress on a material in an elastic regime, caused by thermal expansion, is

$$S = \alpha Y \delta T, \tag{6}$$

where Y is Young's modulus, α is the thermal expansivity, and δT is the temperature change. In this work, we are assuming that the properties of the asteroidal surface are compatible with those of typical carbonaceous chondrites, which are characterized by values of $Y = (7–20) \times 109$ Nm^{-2} (Pohl and Britt 2020) and $\alpha = 10^{-6}$ K^{-1} (Opeil et al. 2020). Hence, replacing $\delta T = 600$ K in Equation (6), we obtain a peak thermal stress of $S = (12) \times 10^6$ Nm^{-2} (12 MPa), experienced on Phaethon at its perihelion. This value is slightly greater than the tensile strengths of terrestrial serpentinite (0.5–5 MPa; C. Burk 1964; R. Altindag and A. Guney 2010) and of materials such as limestone and shale (1–12 MPa; H. P. Sanio 1985; C.-S. Chen et al. 1998). Also on Bennu, where dust activity is observed, the surface stresses range from ~2 to 5 MPa (J. L. Molaro et al. 2020), and weaker stresses have been estimated (0.2 MPa) on (162173) Ryugu boulders as well (M. Grott et al. 2019). Both asteroids are made of carbonaceous material. However, in terrestrial environments, the threshold for triggering subcritical crack growth requires a factor that is ~10%–20% of the material fracture toughness (B. K. Atkinson 1984). Nevertheless, our thermal model suggests the presence of stresses greater by 20% than the tensile strength, indicating that thermal fracturing can be active on Phaethon and could contribute to the production of small particles on Phaethon.

7.1.1. Comparison with Previous VIS–NIR Analysis and the IR Spectrum Results

For comparison, Licandro et al. (2007) suggested compositional similarities with aqueously altered CI/CM meteorites—hydrated silicates such as montmorillonite and antigorite—and they identified as closer matches the Y-86720 samples and Ivuna heated to 700°C. Clark et al. (2010) matched the Phaethon VIS–NIR spectrum (presented by Binzel et al. 2001; F. De Meo et al. 2009) with CK chondrites and a mineral mix of chlorite and carbon. M. Lazzarin et al. (2019) identified Y-82162, Ivuna heated to 700°C, Murchison heated to 900°C, and Murchison IOM (55–63 and 90–106 μm) as possible analogs.

Table 4
Top 10 Meteorites Similar to the Northern Region of Phaethon

Meteorites Similar to the Northern Region of Phaethon							
Position	Name ID	Slope 0.55–0.7	Slope 0.4–0.55	Specimen Name	Specimen Description	Particle Size (μm)	Distance
1	c1mb64j3	-0.09 ± 0.01	-0.13 ± 0.01	Murchison	Heated for one week at 900°C in 10^−5 atm H2	45–75	0.328
2	c2mb64j4	-0.09 ± 0.01	-0.13 ± 0.01	Murchison	Heated for one week at 900°C in 10^−5 atm H2	75–125	0.332
3	c1mb64j4	-0.12 ± 0.01	-0.06 ± 0.02	Murchison	Heated for one week at 900°C in 10^−5 atm H2	75–125	0.334
4	c1mb64j2	-0.06 ± 0.01	-0.12 ± 0.01	Murchison	Heated for one week at 900°C in 10^−5 atm H2	25–45	0.353
5	cmmb64	-0.04 ± 0.01	-0.17 ± 0.01	Murchison	Heated for one week at 900°C in 10^−5 atm H2	63–125	0.361
6	c1mb19c	-0.13 ± 0.02	0.08 ± 0.01	Y-82162,76	Carbonaceous Chondrite CI Unusual	63–125	0.422
7	ccmb19	-0.29 ± 0.02	0.18 ± 0.03	Y-82162,79	CI Unusual—chip with light surficial (weathering) coating	Fresh interior of chip	0.44
8	cemp18	-0.22 ± 0.01	-0.69 ± 0.02	Ivuna	Heated in a vacuum cell with Carbon rod for one week at 700°C	0–125	0.479
9	c1mb64j1	0.04 ± 0.01	-0.04 ± 0.01	Murchison	Heated for one week at 900°C in 10^−5 atm H2	0–25	0.480
10	cfmb64	-0.04 ± 0.02	0.08 ± 0.02	Murchison	Heated for one week at 900°C in 10^−5 atm H2	0–63	0.481

Note. This table lists the top 10 meteorites that most closely match the spectral properties of the northern region of Phaethon. The table includes the position in the list, meteorite name ID from RELAB, spectral slope in the 0.55–0.7 μm and 0.4–0.55 μm ranges, specimen name and description, particle size, and calculated distance from the northern region.

Table 5
Top 10 Meteorites Similar to the Equatorial Region of Phaethon

Meteorites Similar to the Equatorial Region of Phaethon							
Position	Name ID	Slope 0.55–0.7	Slope 0.4–0.55	Specimen Name	Specimen Description	Particle Size (μm)	Distance
1	c1mb64j3	-0.09 ± 0.01	-0.13 ± 0.01	Murchison	Heated for one week at 900°C in 10^−5 atm H2	45–75	0.348
2	c2mb64j4	-0.09 ± 0.01	-0.13 ± 0.01	Murchison	Heated for one week at 900°C in 10^−5 atm H2	75–125	0.351
3	c1mb64j4	-0.12 ± 0.01	-0.06 ± 0.01	Murchison	Heated for one week at 900°C in 10^−5 atm H2	75–125	0.360
4	c1mb64j2	-0.06 ± 0.01	-0.12 ± 0.01	Murchison	Heated for one week at 900°C in 10^−5 atm H2	25–45	0.372
5	cmmb64	-0.04 ± 0.01	-0.17 ± 0.01	Murchison	Heated for one week at 900°C in 10^−5 atm H2	63–125	0.376
6	cemp18	-0.22 ± 0.01	-0.69 ± 0.02	Ivuna	Heated in a vacuum cell with Carbon rod for one week at 700°C	0–125	0.443
7	c1mb19c	-0.13 ± 0.02	0.08 ± 0.01	Y-82162	Carbonaceous Chondrite CI Unusual	63–125	0.457
8	ccmb19	-0.28 ± 0.02	0.18 ± 0.03	Y-82162	CI Unusual—chip with light surficial (weathering) coating	Fresh interior of chip	0.485
9	c1mb64j1	0.04 ± 0.01	-0.04 ± 0.01	Murchison	Heated for one week at 900°C in 10^−5 atm H2	0–25	0.502
10	cfmb64	-0.04 ± 0.02	0.08 ± 0.02	Murchison	Heated for one week at 900°C in 10^−5 atm H2	0–63	0.512

Note. This table lists the top 10 meteorites that most closely match the spectral properties of the equatorial region of Phaethon. The table includes the position in the list, meteorite name ID from RELAB, spectral slope in the 0.55–0.7 μm and 0.4–0.55 μm ranges, specimen name and description, particle size, and calculated distance from the equatorial region.

Table 6
Top 10 Meteorites Similar to the Southern Region of Phaethon

Meteorites Similar to the Southern Region of Phaethon							
Position	Name ID	Slope 0.55–0.7	Slope 0.4–0.55	Specimen Name	Specimen Description	Particle Size (μm)	Distance
1	cbmb19	-0.67 ± 0.01	-0.77 ± 0.01	Y-82162	CI Unusual—chip with light surficial (weathering) coating	Larger chip	0.201
2	cemp18	-0.22 ± 0.01	-0.69 ± 0.02	Ivuna	Heated in a vacuum cell with Carbon rod for one week at 700°C	0–125	0.254
3	camb19	-0.78 ± 0.03	-0.75 ± 0.03	Y-82162	CI Unusual—chip with light surficial (weathering) coating	Small chip	0.308
4	cmmb64	-0.04 ± 0.01	-0.17 ± 0.01	Murchison	Heated for one week at 900°C in 10^−5 atm H2	63–125	0.729
5	c1mb64j3	-0.09 ± 0.01	-0.13 ± 0.01	Murchison	Heated for one week at 900°C in 10^−5 atm H2	45–75	0.736
6	c2mb64j4	-0.09 ± 0.01	-0.13 ± 0.01	Murchison	Heated for one week at 900°C in 10^−5 atm H2	75–125	0.737
7	c1mb64j2	-0.06 ± 0.01	-0.12 ± 0.01	Murchison	Heated for one week at 900°C in 10^−5 atm H2	25–45	0.752
8	c1mb64j4	-0.12 ± 0.01	-0.06 ± 0.01	Murchison	Heated for one week at 900°C in 10^−5 atm H2	75–125	0.779
9	c1mb64j1	0.04 ± 0.01	-0.04 ± 0.01	Murchison	Heated for one week at 900°C in 10^−5 atm H2	0–25	0.879
10	c1mb19c	-0.13 ± 0.02	0.08 ± 0.01	Y-82162,79	Carbonaceous Chondrite CI Unusual	63–125	0.905

Note. This table lists the top 10 meteorites that most closely match the spectral properties of the southern region of Phaethon. The table includes the position in the list, meteorite name ID from RELAB, spectral slope in the 0.55–0.7 μm and 0.4–0.55 μm ranges, specimen name and description, particle size, and calculated distance from the southern region.

Our analysis of Phaethon reinforces previous findings regarding its observed spectral properties in the VIS and NIR (with a possible link to heated CI/CM). Earlier studies identified meteorite analogs for Phaethon by fitting spectra from a limited number of observations, often just a single observation, and without photometric corrections. In contrast, our work compiles all available spectral observations, in an effort to localize the observed surface regions. After applying photometric corrections, we use a scatter plot of two spectral parameters (the slopes between 0.55–0.7 μm and 0.4–0.55 μm) to identify a spectroscopic meteorite analog.

Regarding the IR spectrum, where molecular vibrations play a key role, E. MacLennan & M. Granvik (2024) reported that Murchison (CM) heated to 900°C provides a good spectral match to Phaethon's IR spectrum. However, as noted by E. MacLennan & M. Granvik (2024), the differing emissivity features near 21 μm effectively rule it out as a potential spectral analog. In contrast, within the CY group, the top three matches were derived from the same meteorite sample: Y-82162 (<63, 63–125 μm, chips).[9] Since IR spectra of Ivuna heated to 700°C are not available, a direct comparison with Phaethon's Spitzer data was not possible. However, we cautiously suggest that the results of E. MacLennan & M. Granvik (2024) are consistent with our findings for the northern region.

If we exclude from our analysis the match with Murchison heated to 900°C, due to the incompatibility at 21 μm (E. MacLennan & M. Granvik 2024), the best fit for the north is Y-82162,76 (63–125 μm).

7.1.2. Comparison with Previous Thermophysical Analysis

In this scenario, the northern region is similar to Y-82162,76 (63–125 μm or the fresh interior chip, considering the very close match); the equatorial region appears to be Ivuna heated to 700°C (0–125 μm) and, if we consider also the second closet match, mixed with Y-82162 (63–125 μm); and the southern region is most likely Ivuna heated to 700°C. We exclude the possibility of a mixture of Ivuna 700°C and Y-82162 for the southern regions, because the latter is about four times farther from the minimum match. This scenario aligns with the findings of E. MacLennan et al. (2022), who, using their TPM and analysis of Phaethon's thermal IR data, identified surface heterogeneity on Phaethon. They found that the northern hemisphere was dominated by coarse-grained or boulder-dominated material (consistent with our finding of particle sizes 63–125 μm or chips), while the southern latitudes are dominated by fine grains (in our case, 0–125 μm, where however fine particles typically dominate spectral properties; J. F. Mustard and J. E. Hays 1997). The equatorial region, from approximately $-30°$ to 10°, likely represents a mixture of the northern and southern terrains (E. MacLennan et al. 2022), as our analysis also suggests.

Given the close similarity between the meteorite matches and the slopes of the northern and equatorial regions—nearly overlapping when considering errors—we cannot rule out a scenario where Phaethon's northern surface contains a mixture of Y-82162 with larger particle sizes and Ivuna heated fine particles. The third match for the northern region corresponds to Ivuna (heated to 700°C, particle size: 0–125 μm).

Insights from the Hayabusa2 and OSIRIS-REx missions, which closely studied the carbonaceous asteroids Ryugu and Bennu, suggest the possibility of mass-wasting processes either toward or away from the equator. For Ryugu, mass movements appear to occur from the equatorial region to the midlatitudes, driven by a lower equatorial geopotential and a likely decrease in rotation period (S. Sugita et al. 2019; S. Watanabe et al. 2019). Conversely, on Bennu, such movements seem to occur in the opposite direction—from midlatitudes to the equator—due to a higher equatorial geopotential and an increasing rotation period (M.C. Nolan et al. 2019; D. N. DellaGiustina et al. 2020; E. R. Jawin et al. 2020).

These observations suggest two plausible scenarios for Phaethon. S. E. Marshall et al. (2022) reported that Phaethon's rotation period is decreasing, which suggests that if its geopotential might resemble that of Ryugu, the mass

[9] The Y-82162 spectrum chip referenced in MacLennan et al. (2024) is identified as bmramp137 (MP-TXH-137). This chip was not utilized in the current study due to its measurement range being limited to NIR–mid-IR only.

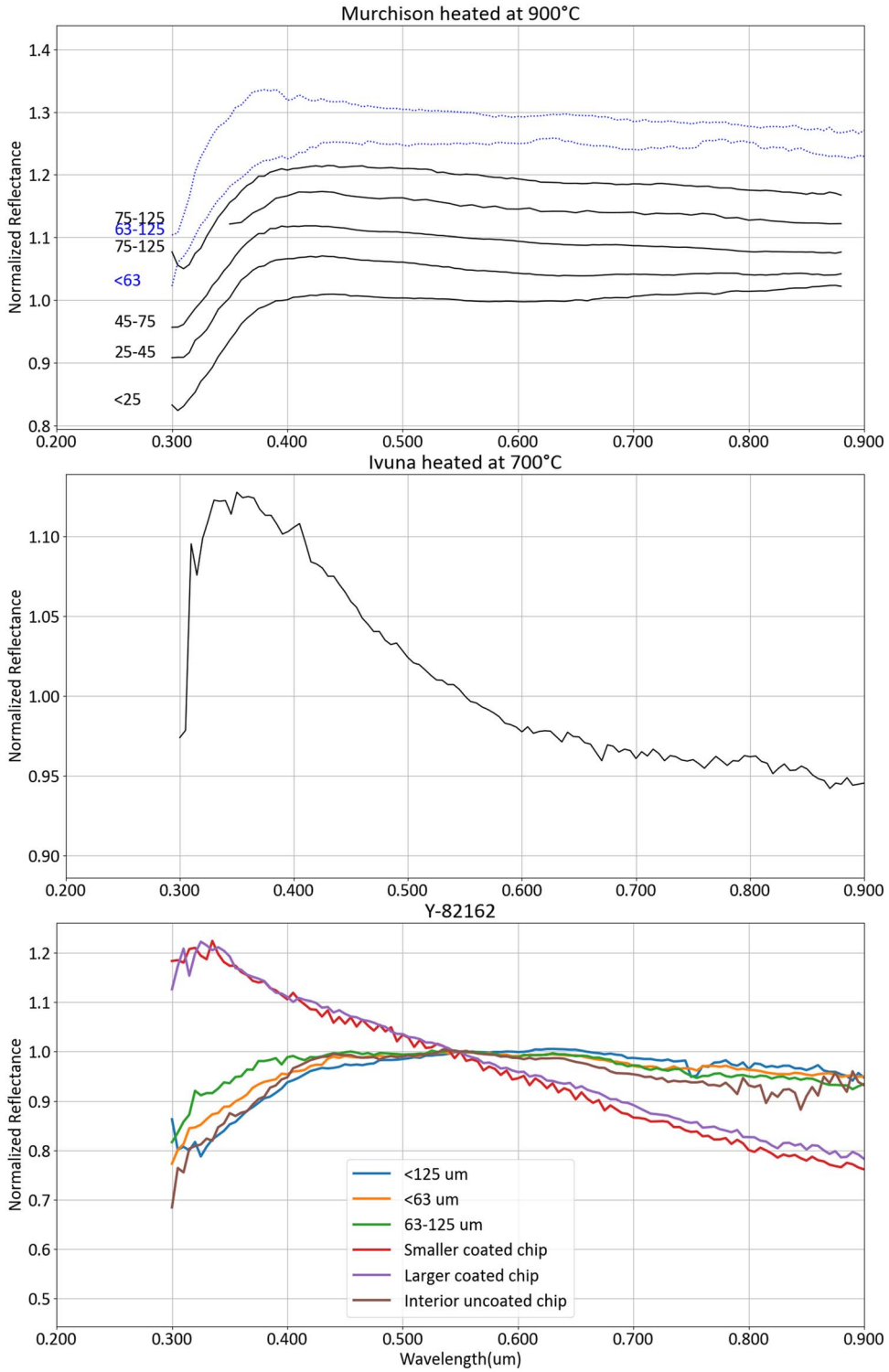

Figure 9. Normalized spectra of the best analogs from RELAB. Top: Murchison meteorite heated to 900°C, shown at various particle sizes (25 μm–125 μm). Middle: Ivuna meteorite heated to 700°C. Bottom: Y-82162 meteorite at different grain sizes and as a chip.

movements are from the equatorial region to midlatitudes. This could result in the northern surface being covered by larger Y-82162 particles overlain by Ivuna heated fine particles, explaining the similar spectral slopes of the northern and equatorial regions. Alternatively, following Bennu's pattern, the equator might consist of mixed materials from both hemispheres. However, these dynamical processes remain under investigation and are beyond the scope of this study.

To summarize, the pole reversal reported by J. Hanuš et al. (2016)—with the north pole being dominant 2000 yr ago and the south pole taking over 4000 and 500 yr ago—could explain the near uniformity in heating temperatures of meteorites that match Phaethon's surface. The southern region is similar to Ivuna, heated to 700°C, while the northern region resembles Y-82162, which experienced long-duration heating at 600–700°C or short-duration heating at 800°C (as suggested

by Akai 1990, 1992, 1994). Currently, the diurnal temperature variation in the southern regions ($\Delta T \sim 600$ K) during perihelion would promote regolith formation and surface renewal, resulting in a particle size of less than 125 μm. In contrast, the northern region is expected to have larger grain sizes (63–125 μm or chips), reinforcing the thermophysical heterogeneity reported by E. MacLennan et al. (2022).

8. Conclusion

Based on the pole solution and shape model provided by J. Hanuš et al. (2016, 2018), and taking thermal inertia into account, we have estimated the surface temperature of Phaethon at perihelion. The analysis reveals a difference in the solar radiation heating between the northern and southern regions. The southern hemisphere reaches a very high surface temperature (∼1050 K), while the northern latitudes experience comparatively lower temperatures (∼760 K).

The daily variation in temperature ($\Delta T \sim 600$ K) can induce thermal stress, which is a potential mechanism for producing small particles and rejuvenating the surface of Phaethon, particularly in the southern regions.

We compiled a database of VIS–NIR spectra of Phaethon, collected from 2007 to 2017, and retrieved their observation geometries. A photometric correction was then applied, providing surface coverage of the entire asteroid. Our analysis revealed a slight latitudinal trend in the spectral slope, correlating with the characteristics of heated aqueously altered carbonaceous meteorites, ruling out the previously suggested links to CK and CV chondrites.

Specifically, a scatter plot of the photometrically corrected spectral slope between 0.55–0.7 μm and 0.4–0.55 μm shows evidence of a surface heterogeneity, with spectral similarities to unusual chondrites and naturally heated Y-82162 (63–125 μm and/or chips) for the northern region. The southern regions exhibit similarities to Ivuna CI chondrites, heated to 700°C (0–125 μm), while the equator appears to be a mixture of the two regions.

These findings support the meteorite match identified in the IR by E. MacLennan & M. Granvik (2024) and reinforce the thermophysical heterogeneity reported by E. MacLennan et al. (2022).

Additionally, the presence of phyllosilicate veins in Y-82162 suggests that hydration has occurred in the parent body, similar to what is found in CI chondrites like Ivuna (Y. Ikeda and K. Makoto et al. 1992). This bolsters the link between Phaethon and heated CI chondrites. It is therefore possible that Phaethon was originally hydrated and, over time, its surface has undergone decomposition and volatile loss, due to dehydration, supporting its connection to the Pallas family, as suggested by Clark et al. (2010).

We point out the necessity of high-resolution imaging to further understand the morphology and peculiarities of Phaethon. The upcoming DESTINY+ mission will provide valuable flyby imaging with a panchromatic telescopic camera (TCAP) and a VIS–NIR multiband camera (MCAP; P. K. Hong et al. 2022; K. Ishibashi et al. 2022), equipped with four bands (i.e., 425, 550, 700, and 850 nm). These observations will allow for a detailed analysis similar to the scatter plot presented here, using data from the Phaethon flyby.

Acknowledgments

The authors wish to thank Beth Ellen Clark and Paul Abell for their helpful critiques that helped to improve this manuscript.

The team thanks Teddy Kareta, Myung-Jin Kim, Javier Licandro, and Monica Lazzarin for sharing Phaethon telescopic data, Josef Hanuš for his support of DAMIT and the Phaethon shape model, and Sean Marshall and Patrick Taylor for their support of radar observations.

This research is financed by PRIN-INAF-2019, F.O: 1.05.01.85.06, "3200 Phaethon Asteroid Composition by Multiple Analysis—PACMAN."

This work is also based on observations made with the Italian Telescopio Nazionale Galileo (TNG) operated on the island of La Palma by the Fondazione Galileo Galilei of the INAF (Istituto Nazionale di Astrofisica) at the Spanish Observatorio del Roque de los Muchachos of the Instituto de Astrofisica de Canarias (Program A36DDT5—P.I.: E. Palomba).

This research utilizes spectra of the NASA RELAB facility at Brown University.

Appendix

This section provides supplementary figures and tables to provide additional context for the analyses presented in this work. Figures A1 and A2 show un-normalized spectra shared by T. Kareta et al. (2018) and un-normalized spectra shared by H. J. Lee et al. (2019). This figure displays un-normalized spectra as shared by them, showcasing the raw spectral data before processing. It highlights intrinsic variations captured during their observations. Table A1 details the positional coordinates of the sub-Earth and subsolar points during the observations. Table A2 presents the spectral slopes measured across various observation sets. The values are categorized by wavelength ranges of 0.55–0.7 μm and 0.4–0.55 μm.

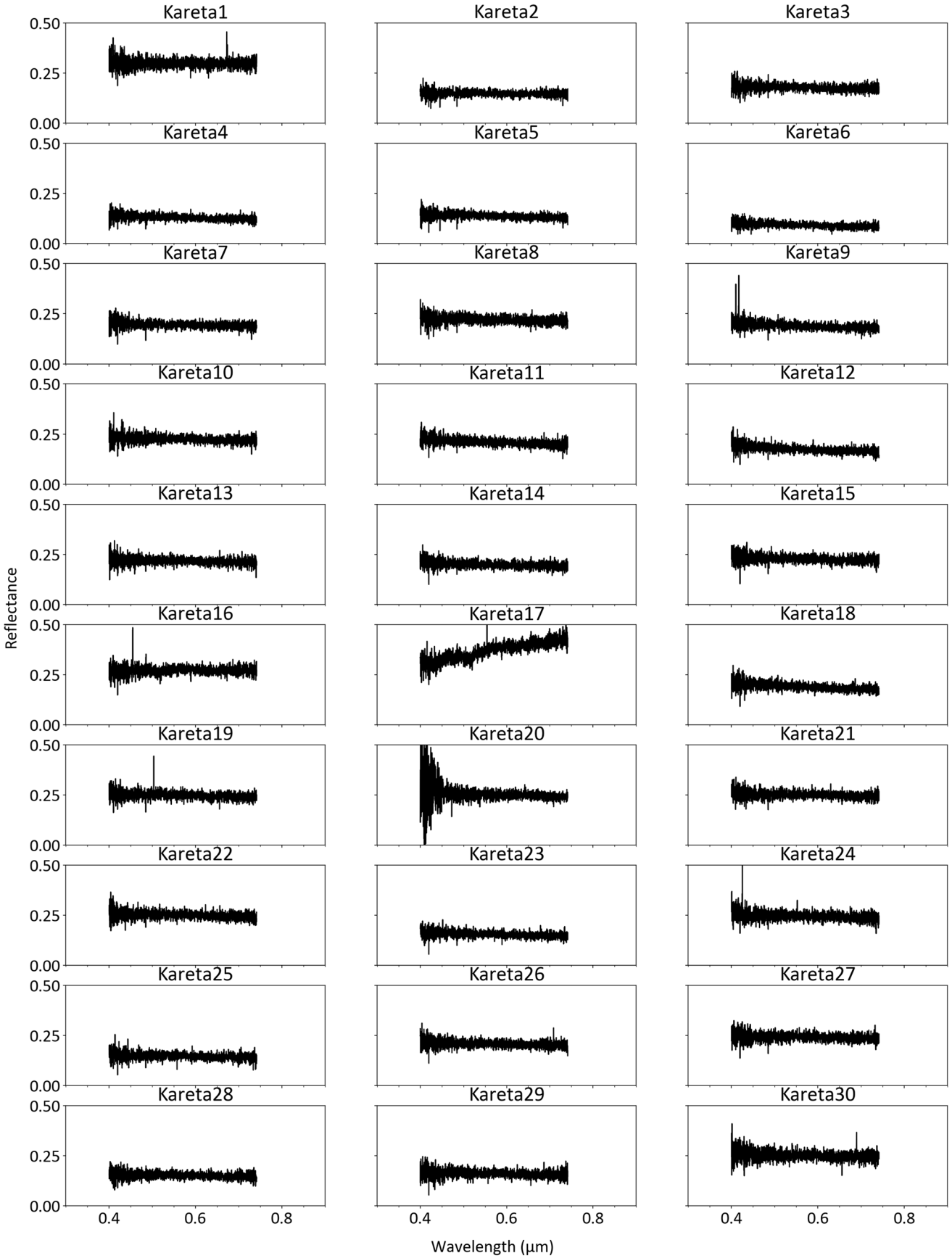

Figure A1. Un-normalized spectra shared by Kareta et al. (2018).

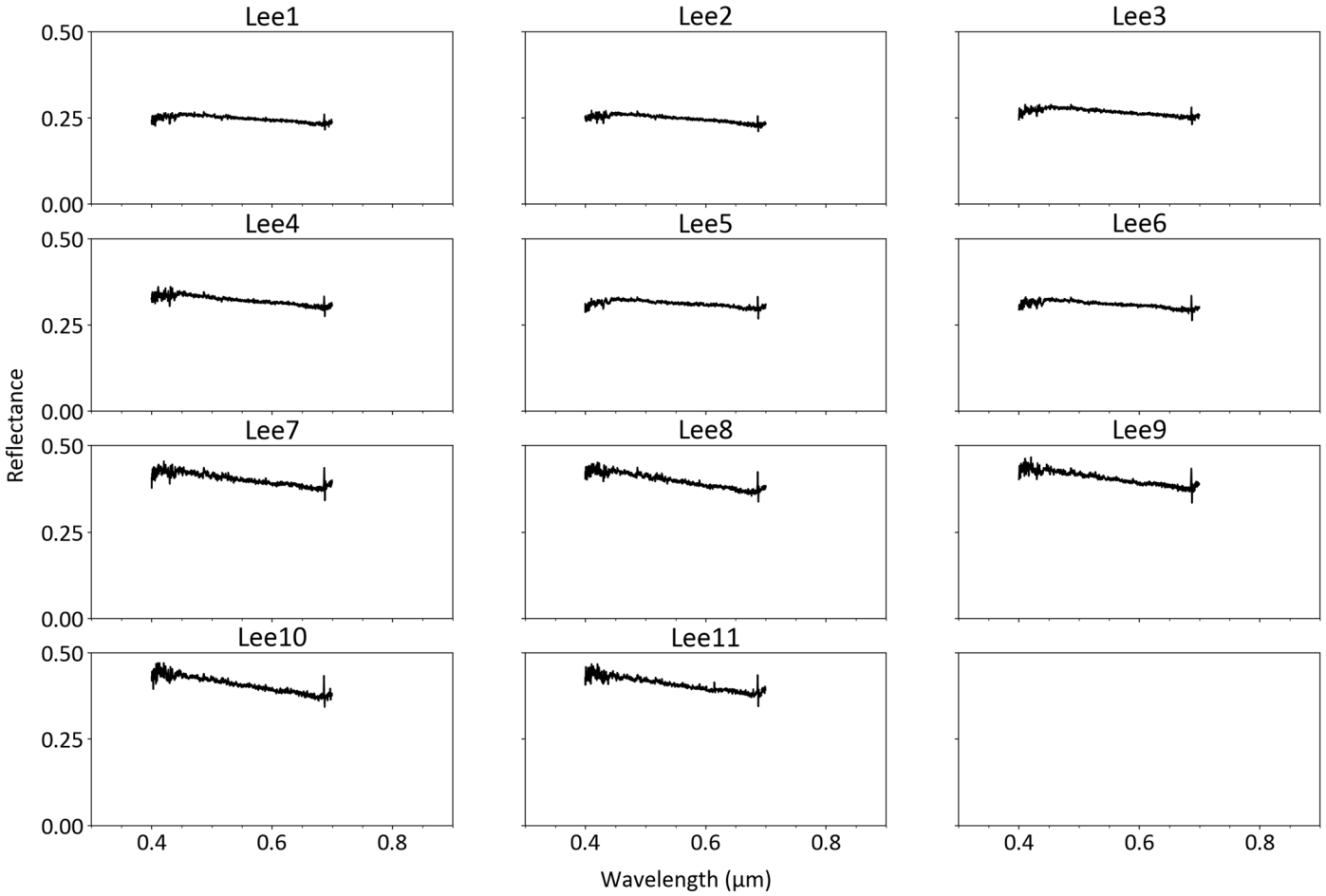

Figure A2. Un-normalized spectra shared by Lee et al. (2019).

Table A1
Observation Coordinates of Sub-Earth and Subsolar Points

Observation	Sub-Earth (lat; long) ± 10°	Subsolar (lat; long) ± 10°
Licandro	(−8; 47)	(−3; 350)
Palomba 1	(−29; 119)	(24; 29)
Palomba 2	(−29; 109)	(24; 19)
Palomba 3	(−29; 100)	(24; 10)
Lazzarin 1	(0; 79)	(23; 19)
Lazzarin 2	(−1; 339)	(23; 279)
Lazzarin 3	(−11; 343)	(23; 273)
Lee 1	(43; 345)	(22; 344)
Lee 2	(43; 335)	(22; 334)
Lee 3	(43; 325)	(22; 324)
Lee 4	(43; 314)	(22; 313)
Lee 5	(43; 304)	(22; 303)
Lee 6	(43; 294)	(22; 293)
Lee 7	(43; 250)	(22; 249)
Lee 8	(43;240)	(22; 239)
Lee 9	(43; 230)	(22; 229)
Lee 10	(43; 220)	(22; 218)
Lee 11	(43; 209)	(22; 208)
Kareta 1	(48; 124)	(20; 161)
Kareta 2	(48; 99)	(20; 136)
Kareta 3	(48; 89)	(20; 127)
Kareta 4	(48; 79)	(20; 117)
Kareta 5	(48; 69)	(20; 106)
Kareta 6	(48; 58)	(20; 96)
Kareta 7	(48; 48)	(20; 85)
Kareta 8	(48; 37)	(20; 75)
Kareta 9	(48; 23)	(20; 60)
Kareta 10	(48; 6)	(20; 44)
Kareta 11	(48; 356)	(20; 34)
Kareta 12	(48; 346)	(20; 23)
Kareta 13	(48; 335)	(20; 13)
Kareta 14	(48; 325)	(20; 3)
Kareta 15	(48; 312)	(20; 350)
Kareta 16	(48; 302)	(20; 340)
Kareta 18	(48; 273)	(20; 310)
Kareta 19	(48; 263)	(20; 300)
Kareta 20	(48; 252)	(20; 290)
Kareta 21	(48; 243)	(20; 280)
Kareta 22	(48; 232)	(20; 270)
Kareta 23	(48; 222)	(20; 259)
Kareta 24	(48; 211)	(20; 249)
Kareta 25	(48; 201)	(20; 239)
Kareta 26	(48; 190)	(20; 228)
Kareta 27	(48; 180)	(20; 218)
Kareta 28	(48; 168)	(20; 206)
Kareta 29	(48; 158)	(20; 196)
Kareta 30	(48; 148)	(20; 185)

Note. This table lists the observed coordinates of the sub-Earth and subsolar points for various observations. The coordinates are given with a ±10° margin for each observation.

Table A2
This Table Presents the Spectral Slopes for Various Observations, Measured in the Ranges of 0.55–0.7 μm and 0.4–0.55 μm.

Observation	Slope 0.55–0.7 μm (μm^{-1} deg^{-1})	Slope 0.4–0.55 μm (μm^{-1} deg^{-1})
Licandro	−0.308 ± 0.001	−0.213 ± 0.005
Palomba 1	−0.436 ± 0.003	−0.624 ± 0.008
Palomba 2	−0.374 ± 0.002	−0.512 ± 0.007
Palomba 3	−0.603 ± 0.002	−1.138 ± 0.005
Lazzarin 1	−0.204 ± 0.006	−0.896 ± 0.008
Lazzarin 2	−0.274 ± 0.002	−0.895 ± 0.005
Lazzarin 3	−0.101 ± 0.006	−0.259 ± 0.004
Lee 1	−0.463 ± 0.004	−0.227 ± 0.013
Lee 2	−0.591 ± 0.004	−0.173 ± 0.013
Lee 3	−0.457 ± 0.003	−0.141 ± 0.014
Lee 4	−0.435 ± 0.004	−0.411 ± 0.009
Lee 5	−0.388 ± 0.005	−0.132 ± 0.015
Lee 6	−0.409 ± 0.005	−0.138 ± 0.012
Lee 7	−0.378 ± 0.008	−0.495 ± 0.007
Lee 8	−0.573 ± 0.006	−0.609 ± 0.005
Lee 9	−0.449 ± 0.006	−0.544 ± 0.005
Lee 10	−0.613 ± 0.005	−0.623 ± 0.006
Lee 11	−0.435 ± 0.005	−0.540 ± 0.004
Kareta 1	−0.066 ± 0.010	−0.159 ± 0.013
Kareta 2	−0.146 ± 0.009	−0.036 ± 0.012
Kareta 3	−0.341 ± 0.009	−0.104 ± 0.010
Kareta 4	−0.501 ± 0.010	−0.430 ± 0.016
Kareta 5	−0.451 ± 0.010	−0.268 ± 0.014
Kareta 6	−0.741 ± 0.017	−0.637 ± 0.019
Kareta 7	−0.241 ± 0.008	−0.324 ± 0.012
Kareta 8	−0.235 ± 0.008	−0.195 ± 0.015
Kareta 9	−0.380 ± 0.008	−0.509 ± 0.014
Kareta 10	−0.335 ± 0.006	−0.085 ± 0.010
Kareta 11	−0.359 ± 0.008	−0.500 ± 0.011
Kareta 12	−0.435 ± 0.010	−0.747 ± 0.011
Kareta 13	−0.308 ± 0.007	0.026 ± 0.009
Kareta 14	−0.267 ± 0.006	−0.408 ± 0.0130
Kareta 15	−0.352 ± 0.008	−0.195 ± 0.011
Kareta 16	−0.217 ± 0.008	0.133 ± 0.018
Kareta 18	−0.497 ± 0.007	−0.571 ± 0.011
Kareta 19	−0.293 ± 0.007	−0.180 ± 0.015
Kareta 20	−0.389 ± 0.008	−0.165 ± 0.011
Kareta 21	−0.369 ± 0.006	−0.182 ± 0.013
Kareta 22	−0.298 ± 0.007	−0.202 ± 0.015
Kareta 23	−0.417 ± 0.008	−0.426 ±0.017
Kareta 24	−0.322 ± 0.006	−0.277 ± 0.013
Kareta 25	−0.399 ± 0.011	−0.113 ± 0.012
Kareta 26	−0.288 ± 0.007	−0.236 ± 0.012
Kareta 27	−0.303 ± 0.006	−0.041 ± 0.011
Kareta 28	−0.394 ± 0.008	−0.035 ± 0.016
Kareta 29	−0.444 ± 0.011	−0.045 ± 0.014
Kareta 30	−0.281 ± 0.010	−0.098 ± 0.011

Note. The slopes are given with their associated uncertainties.

ORCID iDs

M. Angrisani https://orcid.org/0000-0002-2178-521X

References

Akai, J. 1990, AMR, 3, 55
Akai, J. 1992, AMR, 5, 120
Akai, J. 1994, AMR, 7, 94
Altindag, R., & Guney, A. 2010, Scientific Research and Essays, 5, 2107
Arai, T. & Destiny+ Science Team 2023, in Lunar and Planetary Science Conf. 54 (Houston, TX: LPIB), 3017
Atkinson, B. K. 1984, JGR, 89, 4077
Binzel, R. P., Harris, A. W., Bus, S. J., & Burbine, T. H. 2001, Icar, 151, 139
Bowell, E. 1989, in Asteroids II, ed. R. P. Binzel et al. (Tucson: Univ. Arizona Press), 524
Burk, C. 1964, Relations Between Government and Sciences (Washington, D. C.: National Academy of Sciences), 188
Chen, C.-S., Pan, E., & Amadei, B. 1998, IJRMM, 35, 43
Ciarniello, M., De Sanctis, M. C., Ammannito, E., et al. 2017, A&A, 598, A130
Clark, B. E., Binzel, R. P., Howell, E. S., et al. 2011, Icar, 216, 462
Clark, B.E., Ziffer, J., Nesvorny, D., et al. 2010, JGRE, 115, E06005
Cloutis, E.A., Hiroi, T., Gaffey, G. J., Alexander, C. M. O. D., & Mann, P. 2011, Icar, 212, 180
Cloutis, E. A., Hudon, P., Hiroi, T., & Gaffey, M. J. 2012a, Icar, 221, 911
Cloutis, E. A., Hudon, P., Hiroi, T., & Gaffey, M. J. 2012b, Icar, 220, 586
Delbo, M., Libourel, G., Wilkerson, J., et al. 2014, Natur, 508, 233
DellaGiustina, D. N., Burke, K. N., Walsh, K. J., et al. 2020, Sci, 370, eabc3660
De Meo, F., Binzel, R. P., Slivan, S. M., & Bus, S. J. 2009, Icar, 202, 160
Ďurech, J., Sidorin, V., & Kaasalainen, M. 2010, A&A, 513, A46
Fornasier, S., Hasselmann, P. H., Deshapriya, J. D. P., et al. 2020, A&A, 644, A142
Grott, M., Knollenberg, J., Hamm, M., et al. 2019, NatAs, 3, 971
Hall, K., & André, M-F. 2001, Geomo, 41, 23
Hanuš, J., Delbo', M., Vokrouhlický, D., et al. 2016, A&A, 592, A34
Hanuš, J., Ďurech, J., Brož, M., et al. 2011, A&A, 530, A134
Hanuš, J., Vokrouhlický, D., Delbo', M., et al. 2018, A&A, 620, L8
Harris, A. W. 1998, Icar, 131, 291
Hiroi, T., Kaiden, H., Imae, N., et al. 2021, PolSc, 29, 100723
Hiroi, T., Zolensky, M. E., Pieters, C. M., & Lipschutz, M. E. 1996, M&PS, 31, 321
Hong, P. K., Ishibashi, K., Suzaki, Y., et al. 2022, in Lunar and Planetary Science Conf. 53 (Houston, TX: LPIB), 1720
Ikeda, Y., & Makoto, K. 1992, Metic, 27, 435
Ishibashi, K., Hong, P., Okamoto, T., et al. 2022, in Lunar and Planetary Science Conf. 53 (Houston, TX: LPIB), 1729
Jawin, E. R., Walsh, K. J., Barnouin, O. S., et al. 2020, JGRE, 125, e2020JE006475
Jewitt, D., & Li, J. 2010, AJ, 140, 1519
Kareta, T., Reddy, V., Hergenrother, C., et al. 2018, AJ, 156, 287
Kim, M. J., Lee, H.-J., Lee, S.-M., et al. 2018, A&A, 619, A123
Lazzarin, M., Petropoulou, V., Bertini, I., et al. 2019, P&SS, 165, 115
Lee, H.-J., Kim, M.-J., Kim, D.-H., et al. 2019, P&SS, 165, 296
Li, J-Y., McFadden, L. A., Parker, J. W., et al. 2006, Icar, 182, 143
Licandro, J., Campins, H., Mothé-Diniz, T., Pinilla-Alonso, N., & de León, J. 2007, A&A, 461, 751
Longobardo, A., Palomba, E., Capaccioni, F., et al. 2017, MNRAS, 469, S346
Longobardo, A., Palomba, E., Ciarniello, M., et al. 2016, Icar, 267, 204
Longobardo, A., Palomba, E., Galiano, A., et al. 2019, Icar, 320, 97
Longobardo, A., Palomba, E., Galiano, A., et al. 2022, A&A, 666, A185
MacLennan, E., Marshall, S., & Granvik, M. 2022, Icar, 388, 115226
MacLennan, E., & Granvik, M. 2024, NatAs, 8, 60
Marshall, S. E., Devogele, M., Taylor, P., et al. 2022, BAAS, 54, 514.07
Marshall, S. E., Taylor, P. A., Rivera-Valentin, E. G., et al. 2021, in IAA Planetary Defense Conference 7 (Vienna: UNOOSA), 231
Masiero, J.R., Wright, E. L., & Mainzer, A. K. 2019, AJ, 158, 97
Molaro, J. L., Walsh, K. J., Jawin, E. R., et al. 2020, NatCo, 11, 2913
Mustard, J. F., & Hays, J. E. 1997, Icar, 125, 145
Nakamura, T. 2005, JMPeS, 100, 260
Nolan, M. C., Howell, E. S., Scheeres, D. J., et al. 2019, GeoRL, 46, 1956
Ohtsuka, K., Nakato, A., Nakamura, T., et al. 2009, PASJ, 61, 1375
Opeil, C. P., Britt, D. T., Macke, R. J., & Consolmagno, G. J. 2020, M&PS, 55, 1
Palomba, E., Migliorini, A., Arai, T., et al. 2018, in COSPAR Scientific Assembly 42 (Pasadena, CA: IPAC), 44
Pohl, L., & Britt, D. T. 2020, M&PS, 55, 962
Rozitis, B., Duddy, S. R., Green, S. F., & Lowry, S. C. 2013, A&A, 555, A20
Sanio, H. P. 1985, International Journal of Rock Mechanics and Mining Sciences & Geomechanics Abstracts, 22, 153
Sugita, S., Honda, R., Morota, T., et al. 2019, Sci, 364, eaaw0422
Takir, D., Kareta, T., Emery, J. P., et al. 2020, NatCo, 11, 2050
Taylor, P. A., Rivera-Valentín, E. G., Benner, L. A. M., et al. 2019, P&SS, 167, 1
Virtanen, P., Gommers, R., Oliphant, T. E., et al. 2020, NatMe, 17, 261
Warner, B. D. 2017, MPBu, 44, 98
Watanabe, S. 2019, Sci, 364, 268